



Revisiting the Space Weather Environment of Proxima Centauri b

Cecilia Garraffo¹ , Julián D. Alvarado-Gómez² , Ofer Cohen³ , and Jeremy J. Drake¹ ¹Center for Astrophysics | Harvard & Smithsonian, 60 Garden Street, Cambridge, MA 02138, USA²Leibniz Institute for Astrophysics Potsdam, An der Sternwarte 16, D-14482 Potsdam, Germany³Lowell Center for Space Science and Technology, University of Massachusetts Lowell, 600 Suffolk Street, Lowell, MA 01854, USA

Received 2022 September 29; revised 2022 November 17; accepted 2022 November 21; published 2022 December 7

Abstract

Close-in planets orbiting around low-mass stars are exposed to intense energetic photon and particle radiation and harsh space weather. We have modeled such conditions for Proxima Centauri b, a rocky planet orbiting in the habitable zone of our closest neighboring star, finding a stellar wind pressure 3 orders of magnitude higher than the solar wind pressure on Earth. At that time, no Zeeman–Doppler observations of the surface magnetic field distribution of Proxima Cen were available and a proxy from a star with a similar Rossby number to Proxima was used to drive the MHD model. Recently, the first Zeeman–Doppler imaging (ZDI) observation of Proxima Cen became available. We have modeled Proxima b’s space weather using this map and compared it with the results from the proxy magnetogram. We also computed models for a high-resolution synthetic magnetogram for Proxima b generated by a state-of-the-art dynamo model. The resulting space weather conditions for these three scenarios are similar with only small differences found between the models based on the ZDI observed magnetogram and the proxy. We conclude that our proxy magnetogram prescription based on the Rossby number is valid, and provides a simple way to estimate stellar magnetic flux distributions when no direct observations are available. Comparisons with models based on the synthetic magnetogram show that the exact magnetogram details are not important for predicting global space weather conditions of planets, reinforcing earlier conclusions that the large-scale (low-order) field dominates, and that the small-scale field does not have much influence on the ambient stellar wind.

Unified Astronomy Thesaurus concepts: [Stellar activity \(1580\)](#); [Stellar winds \(1636\)](#); [Space weather \(2037\)](#)

1. Introduction

Extensive research has been directed toward understanding the conditions of close-in planets orbiting M dwarfs. These planets are by far the most abundant kind of detected exoplanet orbiting in the temperature-based definition of the habitable zone (HZ). Due to the low luminosity of M dwarfs, their HZ resides very close to the host star (e.g., Kopparapu et al. 2013, 2014; Shields et al. 2016). Low-mass stars are typically magnetically more active than higher-mass stars, and remain active for much longer (e.g., Reiners & Basri 2008; Wright et al. 2011; Jackson et al. 2012; Cohen & Drake 2014; Davenport et al. 2019). The associated coronal and chromospheric integrated high-energy radiation can evaporate planetary atmospheres and poses a risk for close-in exoplanets. In addition, the pressure of the stellar wind also scales with magnetic activity (e.g., as $\dot{M}_\star \propto L_X^{1.34}$, Wood et al. 2005; Vidotto et al. 2014; Garraffo et al. 2015a, 2017) and therefore close-in planets are expected to experience stronger stellar winds for longer evolutionary timescales, which puts their atmospheres at risk of being stripped.

Proxima Centauri b (Proxima b hereafter) is a rocky planet orbiting in the “habitable zone” of Proxima Centauri, our closest neighboring star at only 1.3 ps from Earth (Anglada-Escudé et al. 2016). Detailed and realistic magnetohydrodynamic (MHD) simulations predicted that Proxima b should experience stellar wind pressures 4 orders of magnitude larger than the solar wind pressure experienced at Earth, together with strong variations of this pressure on timescales as short as a day

(Garraffo et al. 2016a). Such simulations also predicted that planets around M dwarfs like Proxima b will suffer from intense Joule heating (Cohen et al. 2014), severe atmospheric loss (Dong et al. 2017; Garcia-Sage et al. 2017), and transitions between sub- and super-Alfvénic wind conditions on timescales as short as a day (Cohen et al. 2014; Garraffo et al. 2017).

The MHD wind simulations on which this work is based were driven by the magnetic fields on the simulated stellar surface (the inner boundary condition). While estimates of the total magnetic flux exist for a number of stars, most stars are either too faint or have surface projected rotation velocities, $v \sin i$, too small, or both, to allow observations of the distribution of the field through the Zeeman–Doppler imaging (ZDI) technique.

To get around the lack of ZDI data for particular stars of interest, theoretical arguments have been made to extrapolate surface magnetic structure observed on one star to another when no observations are available. This criterion uses similarities in either spectral type or in the Rossby number—the ratio of rotation period to convective turnover time commonly used as a simple dynamo number (e.g., Noyes et al. 1984; Wright et al. 2011)—as an indicator for the large-scale structure of the magnetic field. This approach was adopted by Garraffo et al. (2016a), who used a magnetogram for the M5 V star GJ 51 from Morin et al. (2010) as a proxy for the surface field of Proxima.

Recently, Klein et al. (2021) reported the first ZDI reconstruction of the large-scale magnetic field of Proxima Cen and provided a rough estimate of its stellar wind structure based on a potential field approximation. The ZDI observations revealed a relatively simple field geometry, with a dominant 135 G dipole component displaced by $\sim 51^\circ$ with respect to the



Original content from this work may be used under the terms of the [Creative Commons Attribution 4.0 licence](#). Any further distribution of this work must maintain attribution to the author(s) and the title of the work, journal citation and DOI.

stellar rotation axis. Due to the extremely slow rotation of Proxima ($P_{\text{rot}} \simeq 89$ days, $v \sin(i) \simeq 0.06 \text{ km s}^{-1}$) and the sparse phase coverage of the observations (10 spectropolarimetric exposures covering one rotation), the resulting ZDI map contains very limited information on other components of the surface field. In contrast, state-of-the-art dynamo models tailored to fully convective stars such as Proxima Cen predict much more complex field distributions, with some solutions producing global-scale mean fields restricted to a single hemisphere (Yadav et al. 2016; Brown et al. 2020). Still, as illustrated by Yadav et al. (2015a), due to cancellation effects and limited spatial resolution, it is expected that a complex magnetic field configuration appears much simpler when reconstructed using ZDI. While the small-scale magnetic field geometry can affect stellar X-ray emission, stellar winds were shown to be dominated by the large-scale structure of the magnetic field: dipole, quadrupole, and octupole modes, in order of importance (Garraffo et al. 2013, 2018; See et al. 2019, 2020). It has been on this basis that many space weather simulations were run with relatively low-resolution ZDI maps (Cohen et al. 2014; Alvarado-Gómez et al. 2016; Garraffo et al. 2017; Alvarado-Gómez et al. 2019b).

The present availability of an observed magnetogram (Klein et al. 2021), a proxy magnetogram (Garraffo et al. 2016a), and a synthetic magnetogram (Yadav et al. 2016) for Proxima Centauri provides a unique opportunity to compare the geometry of the three, as well as wind model solutions and space environment conditions derived from them. Comparing the winds obtained from these three magnetograms is also important to validate assumptions made and proxy magnetograms adopted when no direct observations are available to drive simulations for a given system.

In this work, we reassess the space weather on Proxima b in the light of the three new magnetograms. Section 2 contains an overview of the Proxima Cen system. We compare the magnetogram structures in Section 3, and we describe our numerical methods in Section 4. In Section 5, we present the resulting space weather conditions on the planet. A summary and conclusions of our work are presented in Section 6.

2. The Proxima Centauri System

Proxima Centauri is a late M dwarf (M5.5) with a mass of $0.122 M_{\odot}$, a radius of $0.154 R_{\odot}$ (Anglada-Escudé et al. 2016), and a rotation period of 83 days (Kiraga & Stepien 2007). Its age has been estimated to be 4.85 Gyr (Ségransan et al. 2003; Kiraga & Stepien 2007; Anglada-Escudé et al. 2016). Proxima Centauri b, a rocky exoplanet orbiting in its HZ, has an orbital radius of just 0.049 au, 20 times smaller than Earth’s orbit. Its mass has been estimated to be at least $1.7 M_{\oplus}$ (Suárez Mascareño et al. 2020) and its equilibrium temperature to be 234 K (Anglada-Escudé et al. 2016), comparable to the Earth’s one of 255 K.

Proxima b has become an icon for potential habitable planets. Its irradiation history has been closely studied in order to assess the climate evolution of the planet (e.g., Ribas et al. 2016; Turbet et al. 2016). Its quiescent space weather conditions have also been modeled in detail and show harsh conditions are expected at the location of the planet, potentially leading to atmospheric stripping, heating, and evaporation (Garraffo et al. 2016a). Kavanagh et al. (2021) further validated

these results by finding a consistent mass loss rate for Proxima Cen.

A magnetic cycle of approximately 7 yr was reported by Wargelin et al. (2017). However, this variability has negligible effects on space weather conditions that have been shown to be very corrosive for a wide range of magnetic activity levels, reaching wind pressures 4 orders of magnitude higher than the solar wind pressure experienced at Earth (Garraffo et al. 2016a, 2017).

Proxima is a flare star (e.g., Fuhrmeister et al. 2011; Vida et al. 2019), and its circumstellar conditions are expected to be even harsher when considering transient effects (Alvarado-Gómez et al. 2019a, 2020b). There are also presently two candidate coronal mass ejections from Proxima, one based on X-ray absorption seen by the Einstein satellite (Haisch et al. 1983; Moschou et al. 2019) and one based on detection of a Type IV radio burst coincident with a white-light flare (Zic et al. 2020).

The presence of a second planet, Proxima c, has been examined (Damasso et al. 2020). If confirmed, this planet would have an estimated mass of $\sim 6\text{--}7 M_{\oplus}$ and a circular orbit of approximately 1.44 au (Benedict & McArthur 2020a, 2020b; Kervella et al. 2020; Gratton et al. 2020). An additional short-period sub-Earth has recently been detected (Faria et al. 2022), with $M \sin i \simeq 0.26 M_{\oplus}$, which becomes the innermost planet in the system at an orbital distance of ~ 0.029 au.

3. The Magnetic Field Distribution of Proxima

Magnetic fields on the surfaces of late-type stars are thought to be the key ingredient driving their winds. Since the energy to drive the wind comes from the magnetic field, it is assumed that the greater the magnetic flux is, the stronger the winds will be. However, it is now recognized that the distribution of the magnetic field over the stellar surface is also a significant factor that plays into the structure of the resulting stellar wind (Vidotto et al. 2014; Garraffo et al. 2015b; Réville et al. 2015).

Zeeman-splitting observations can be used to estimate the stellar magnetic flux. Reiners & Basri (2008) have estimated the average field of Proxima Centauri to be $\sim 600G$. Observations of the magnetic field geometry on the stellar surface are instead sparse since they require ZDI, which is a more demanding method that requires the source star to be comparatively bright and to rotate fast enough for a Doppler shift-modulated magnetic signature to be detected (e.g., Donati & Landstreet 2009). Realistic MHD simulations of stellar winds are driven by the magnetic map of the stellar surface field (a “magnetogram”). Therefore, the main limitation on obtaining these maps for stars translates to a limitation in modeling their winds, mass loss, and angular momentum loss, which are all relevant for a number of astrophysical phenomena, like stellar spin down and evolution, and the space weather of exoplanets.

Stellar magnetic activity is driven by the dynamo processes, fueled by rotation such that faster rotation results in stronger magnetic activity (e.g., Kraft 1967; Skumanich 1972; Vaiana et al. 1981). Additionally, X-ray observations, in concert with magnetic activity indicators at other wavelengths, reveal a strong correlation between magnetic activity and the Rossby number ($Ro = P_{\text{rot}}/\tau$, where P_{rot} is rotation period and τ the convective turnover time; see, e.g., Noyes et al. 1984; Pizzolato et al. 2003; Wright et al. 2011). It has recently been realized that the distribution of magnetic fields on the stellar surface

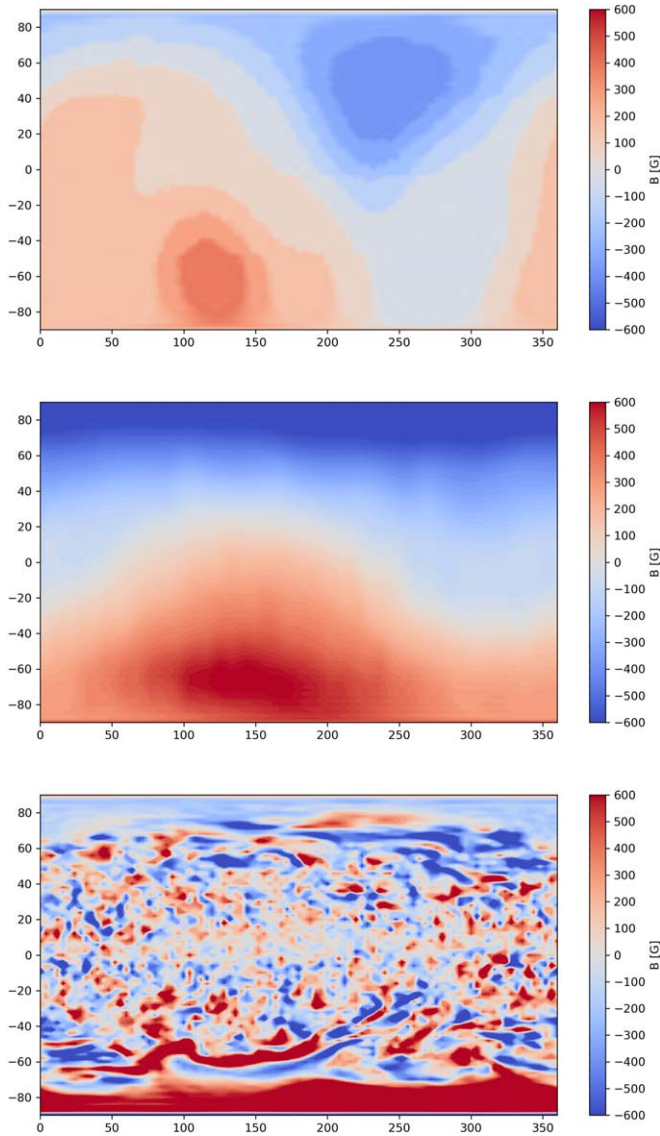


Figure 1. The different Proxima magnetograms used in this study. From top to bottom: the observed ZDI magnetogram from Klein et al. (2021), the proxy magnetogram for Proxima Cen from Garraffo et al. (2016a), and the synthetic magnetogram from the dynamo simulations of Yadav et al. (2016).

also seems to be governed by Ro (Garraffo et al. 2018, see also Morin et al. 2010; Gastine et al. 2013). Using that information, one can choose a suitable representative proxy magnetogram obtained for a star with similar stellar properties and Ro as the star of interest when ZDI observations are not available. That technique has been used several times, allowing simulations of the space environment of Proxima Centauri (Garraffo et al. 2016a), TRAPPIST-1 (Garraffo et al. 2017), Barnard’s Star (Alvarado-Gómez et al. 2019b), and TOI-700 (Cohen et al. 2020).

The proxy GJ 51 magnetogram employed by Garraffo et al. (2016a) is compared with the newly observed Proxima ZDI map by Klein et al. (2021), and the synthetic magnetogram generated by the Yadav et al. (2016) dynamo model in Figure 1. We see that the observed and the proxy ones are similar, both in structure and in magnetic field strengths. They are both dominantly dipolar and with a maximum field strength of ~ 600 G. The dynamo-simulated magnetogram has, as expected, much higher resolution than the observed ones (note

that the proxy magnetogram is also an observed ZDI map for a different star). There is a lot of small structure and concentrated field. The field strength in the dynamo model has been normalized to a $Br\text{-max} = 600$ G. This has been made not only to make it more comparable to the observed ones, but also because the original Br from the simulation is extracted at $R = 0.95 R_{\text{star}}$ and therefore with much larger field strengths, due to the greater ambient pressure and concentration of field. The total magnetic flux in each of the magnetograms is $\Phi_T = 2.0 \times 10^{25}$ Mx (observed), 4.25×10^{25} Mx (proxy), and 4.4×10^{25} Mx (dynamo simulation).

In order to compare the magnetic complexity of the magnetograms, we performed spherical harmonic decomposition and calculated the average large-scale order, n_{av} , as in Garraffo et al. (2016b), by taking the weighted average of the magnetic multipolar order,

$$n_{\text{av}} = \sum_{n=0}^{n_{\text{max}}} \frac{n\Phi_n}{\Phi_T} \quad (1)$$

where n is the multipolar order, and Φ_n is the magnetic flux in each term of the decomposition. We consider the large-scale structure to be all orders lower than or equal to 7. We find that the dominant large-scale orders are $n_{\text{av}} = 1.7$, 1.5, and 3.8 for the observed ZDI, the Proxy, and the synthetic magnetograms, respectively. In accord with the appearance of being much more high-order dominated, the model magnetogram is then significantly more complex on average than the observed ones.

4. Wind Model

We use the AWSOM model (van der Holst et al. 2014) to simulate the stellar corona and stellar wind. The model uses the input magnetogram to specify the radial magnetic field distribution and to calculate the potential magnetic field in the whole domain. This three-dimensional field serves as the initial potential magnetic field in the simulation. The model then solves the nonideal MHD equations (the conservation of mass, momentum, magnetic induction, and energy), taking into account Alfvén wave coronal heating and solar wind acceleration as additional momentum and energy terms. It also accounts for radiative cooling and electron heat conduction. The final steady-state solution is the nonpotential, energized corona, and accelerated stellar wind, where the overall structure of the wind solution follows the structure of the input magnetogram field. Numerical validation of the AWSOM/BATSRUS model, including standard numerical tests and grid convergence have been presented in Powell et al. (1999), Toth et al. (2005, 2012), and van der Holst et al. (2014). Validation of the model against solar and solar wind observations has been presented in (e.g., van der Holst et al. 2014; Sachdeva et al. 2019). An initial grid refinement is applied with a radially stretched grid. This creates a grid with a smallest grid size of $\Delta x = 0.026R_*$ near the inner boundary, and a large grid size of $\Delta x = 0.5R_*$ near the outer boundary. All three cases were simulated with an identical grid to remove any possible impact of the grid on the results. We refer the reader to van der Holst et al. (2014) for a complete description of the model.

The wind model has two main free parameters that control the solution (other than the input magnetogram). One is the Poynting flux that is provided at the inner boundary. This parameter dictates how much wave energy is supplied at the footpoint of a coronal magnetic field line. The other parameter

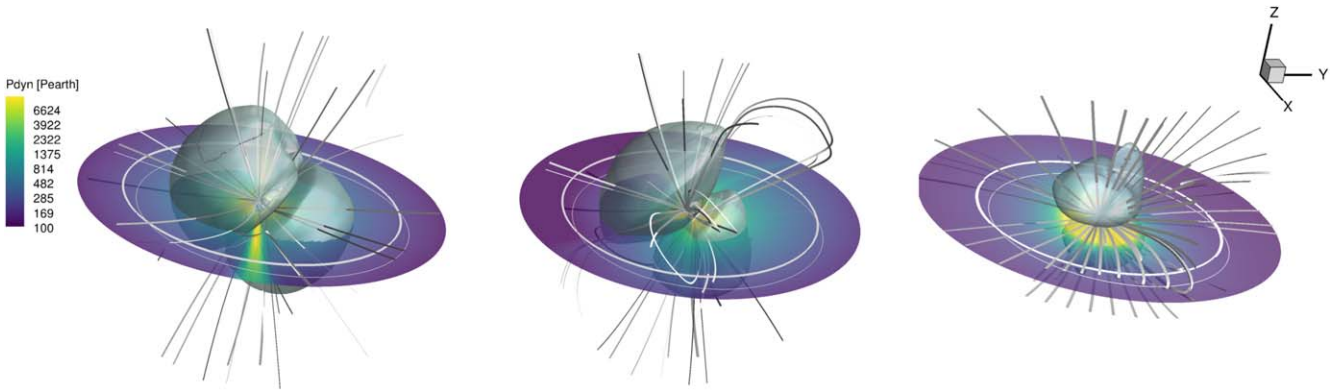


Figure 2. Three-dimensional stellar wind simulations of Proxima Centauri driven by the observed ZDI magnetogram (left), the proxy magnetogram (middle), and the synthetic dynamo-generated magnetogram (right). The equatorial plane is colored according to dynamic wind pressure normalized to the solar wind pressure at 1 au. The simulated orbits for Proxima b are in white (the thick line is the circular orbit). The gray shaded surface denotes the Alfvén surface. The colored domain has a radius of $110R_*$ ($16.9R_\odot$).

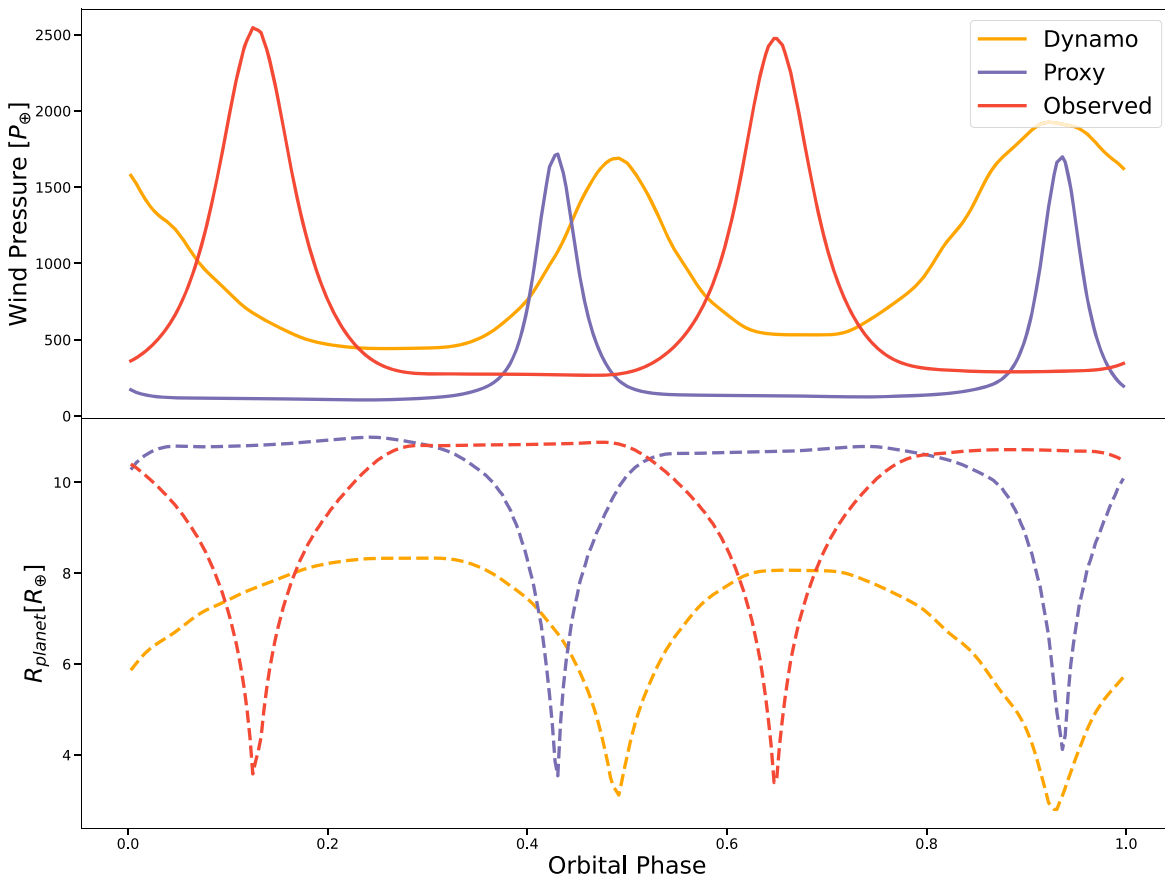


Figure 3. Top: dynamic wind pressure normalized to the solar wind pressure at Earth using the proxy map (purple), the Proxima Centauri observed map (red), and the dynamo map (orange). Bottom: magnetospheric standoff distance for the same cases.

is related to the proportionality constant that controls the dissipation of the Alfvén wave energy into the coronal plasma. For consistency, we use the same set of parameters for all three input magnetograms, where the Poynting flux (per unit magnetic field) value is $1.1 \times 10^6 \text{ [W m}^{-2} \text{ T}^{-1}]$, and the dissipation parameter equals $6 \times 10^5 \text{ [m}\sqrt{\text{T}}]$. The former is the same value that is typically used for solar simulations, while the latter is slightly higher due to the fact that the stellar magnetic field of Proxima Centauri is much stronger than that of the Sun (van der Holst et al. 2014; Sachdeva et al. 2019).

Wind models were computed for each of the three magnetograms and wind conditions were extracted at the putative orbit of Proxima b. Neither the orbital eccentricity nor the inclination of Proxima b with respect to the stellar rotation axis are known. We extracted conditions at an orbital inclination of 0° and for eccentricities of $e = 0$ and 0.2 . This differs from Garraffo et al. (2016a), who examined 10° and 60° inclinations; however, the difference between conditions at 0° and 10° inclinations is negligible.

5. Results and Discussion

Wind model results for the three magnetograms showing the wind dynamic pressure, some selected magnetic field lines, and the Alfvén surface are illustrated in Figure 2.

Despite the differences in the magnetograms, the wind solutions in all three scenarios have similar structures although there are some differences in dynamic pressures. The latter is borne out more clearly in Figure 3, showing the dynamic pressure at the orbital distance of Proxima b as a function of the orbital phase for each model wind solution (solid lines). As expected, the results for eccentricities $e = 0$ and 0.2 are very similar and, therefore, are not illustrated. The main differences between the three solutions are due to the different orientations of the dipolar magnetic axis with respect to the orbital plane axis. This can also be seen clearly from Figure 2. In the case driven by the dynamo-generated magnetogram, the two axes are closely aligned. Therefore, the orbital plane is essentially the same as the current sheet plane. Note that the phases are arbitrarily chosen. In all three cases, the orbit of Proxima b lies outside the stellar Alfvén radius and experiences supersonic wind conditions.

The similar wind solutions from such different magnetograms—observed and proxy versus simulated—does not come as a surprise since, as discussed in Section 1, it is the large-scale structure (dipole, quadrupole and octupole components) that determines the wind structure. The sizes of the resulting Alfvén surfaces are comparable for the three cases: very similar for ZDI and proxy driven simulations, and smaller for the dynamo-simulated scenario. Once again, this latter result is expected when the field is higher-order (Garraffo et al. 2016b). We find that the wind speeds and wind densities and, therefore, the wind pressures are very similar in all cases (see Figures 2 and 3).

The average wind pressures for the three cases fall in the range 100–300 times the solar wind pressure at Earth. The variability is similar for the three cases, although more pronounced for the proxy and ZDI magnetic maps. The reason for this is that, in these cases, the orbits experience two crossings of the astrospheric current sheet per orbit (where the density is higher due to the mostly dipolar large-scale magnetic field). This is a consequence of the inclination of the magnetic axis with respect to the rotation axis. For the dynamo driven solution, both axes are aligned and, therefore, the variability is smaller.

It is important to note that these are steady-state simulations and reflect the quiescent stellar winds for each magnetogram. However, changes in the surface magnetic field of Proxima Centauri are expected to arise from its 7 yr magnetic cycle. Those changes amount to about a factor 2 in the X-ray emission (Wargelin et al. 2017). Based on the empirical relation between unsigned magnetic flux, Φ , and X-ray luminosity, L_X , found by Pevtsov et al. (2003), $L_X \propto \Phi^{1.13}$, the expected change in magnetic flux over the cycle is also expected to be approximately a factor of 2. This is similar to the difference in total magnetic flux between the observed and proxy magnetograms described in Section 3. Magnetic cycle-induced variations in space weather in the Proxima system are not expected to be severe (see Alvarado-Gómez et al. 2020a).

In order to get a better idea of how the different wind conditions through the orbit and due to the different magnetograms might affect Proxima b, we calculate the size of the planetary magnetosphere along its orbit, assuming a

planetary surface magnetic field of 0.1 G as estimated by Zuluaga & Bustamante (2018). We use the conventional equation for the magnetopause standoff distance, R_{mp} , which equates the magnetosphere dipolar field magnetic pressure with the wind’s dynamic pressure, P_{wd} (e.g., Kivelson & Russell 1995; Gombosi 2004):

$$\frac{R_{mp}}{R_p} = \left[\frac{B_p^2}{4\pi P_{wd}} \right]^{1/6}, \quad (2)$$

where R_p and B_p are the planetary radius and surface magnetic field strength, respectively. Figure 3 (dashed lines) shows the size of the resulting magnetosphere for the three cases. It can be seen that the magnetosphere size changes inversely with the stellar wind pressure, and the overall size of the magnetosphere is not that different for all three cases.

It is of interest to compare the results from the detailed MHD simulations presented here with the potential field-based estimates of conditions by Klein et al. (2021). Klein et al. (2021) assumed a constant stellar wind speed, and concluded that stellar wind variations around Proxima Centauri b should be roughly constant. In realistic simulations we find instead that different stellar wind sectors can have quite different conditions, as previously noted in Garraffo et al. (2016a). Our MHD wind solution finds quite large wind dynamic pressure variations along the planetary orbit amounting to factors of 3 (the dynamo model magnetogram) and factors of 10 (the observed magnetogram), which would occur on timescales of a day or less.

Klein et al. (2021) suggest that Proxima b could sustain a magnetosphere of radius 2–3 R_p , based on planetary parameters from Ribas et al. (2016). Those authors investigated magnetic fields of $B_p = B_\oplus$ and $0.2B_\oplus$, where B_\oplus corresponds to the field strength of the Earth. The value assumed for the Earth’s magnetic field strength was not stated, but is commonly assumed to be 0.3 G (e.g., Kivelson & Russell 1995; Gombosi 2004). This would correspond to field strengths in the Klein et al. (2021) calculations of 0.3 and 0.06 G, which span the value of 0.1 G assumed here. Here, we find the magnetopause standoff distance that strongly varies with time, with values ranging between approximately $3R_p$ and $11R_p$, depending on the orbital phase and wind solution.

6. Summary and Conclusions





The main conclusion from this work is that the differences between the three magnetogram scenarios explored are at the detail level, and not significant for a description of the global space weather. Such differences are also within the range of expected magnetic-cycle variability of Proxima Centauri.

The proxy magnetogram criteria used by Garraffo et al. (2016a, 2017) results in a space weather environment not significantly different than the one resulting from the observed ZDI magnetogram. The reason is that the large-scale magnetic field distribution on the stellar surface is mainly dictated by the stellar rotation period and mass, through the Rossby number prescription. Based on those stellar parameters one can estimate the magnetic flux and the order of the magnetic field distribution. This validates the proxy method and justifies the use of a representative ZDI observation for a star for which no ZDI is available. This will allow the community to make advances toward reliably assessing the space weather conditions on a vast number of interesting systems.

Our results also support the dynamo simulations by Yadav et al. (2015b). The synthetic magnetograms resulting from the dynamo simulations look significantly different to the observed ZDI maps. However, the fact that they lead to a similar global space weather suggests that they capture the important large-scale distribution of the field.

We thank the anonymous referee for a very thorough, useful and constructive report. CG and JJD were supported by NASA contract NAS8-03060 to the *Chandra X-ray Center*. Simulation results were obtained using the (open source) Space Weather Modeling Framework, developed by the Center for Space Environment Modeling, at the University of Michigan with funding support from NASA ESS, NASA ESTO-CT, NSF KDI, and DoD MURI. The simulations were performed on NASA's Pleiades cluster (under SMD-17-1330 and SMD-16-6857), as well as on the Massachusetts Green High Performance Computing Center (MGHPCC) cluster.

ORCID iDs

Cecilia Garraffo  <https://orcid.org/0000-0002-8791-6286>
 Julián D. Alvarado-Gómez  <https://orcid.org/0000-0001-5052-3473>
 Ofer Cohen  <https://orcid.org/0000-0003-3721-0215>
 Jeremy J. Drake  <https://orcid.org/0000-0002-0210-2276>

References

- Alvarado-Gómez, J. D., Drake, J. J., Garraffo, C., et al. 2020a, *ApJL*, **902**, L9
 Alvarado-Gómez, J. D., Drake, J. J., Fraschetti, F., et al. 2020b, *ApJ*, **895**, 47
 Alvarado-Gómez, J. D., Drake, J. J., Moschou, S. P., et al. 2019a, *ApJL*, **884**, L13
 Alvarado-Gómez, J. D., Garraffo, C., Drake, J. J., et al. 2019b, *ApJL*, **875**, L12
 Alvarado-Gómez, J. D., Hussain, G. A. J., Cohen, O., et al. 2016, *A&A*, **594**, A95
 Anglada-Escudé, G., Amado, P. J., Barnes, J., et al. 2016, *Natur*, **536**, 437
 Benedict, G. F., & McArthur, B. E. 2020a, *RNAAS*, **4**, 46
 Benedict, G. F., & McArthur, B. E. 2020b, *RNAAS*, **4**, 86
 Brown, B. P., Oishi, J. S., Vasil, G. M., Lecoanet, D., & Burns, K. J. 2020, *ApJL*, **902**, L3
 Cohen, O., & Drake, J. J. 2014, *ApJ*, **783**, 55
 Cohen, O., Drake, J. J., Gloer, A., et al. 2014, *ApJ*, **790**, 57
 Cohen, O., Garraffo, C., Moschou, S.-P., et al. 2020, *ApJ*, **897**, 101
 Damasso, M., Del Sordo, F., Anglada-Escudé, G., et al. 2020, *SciA*, **6**, eaax7467
 Davenport, J. R. A., Covey, K. R., Clarke, R. W., et al. 2019, *ApJ*, **871**, 241
 Donati, J. F., & Landstreet, J. D. 2009, *ARA&A*, **47**, 333
 Dong, C., Lingam, M., Ma, Y., & Cohen, O. 2017, *ApJL*, **837**, L26
 Faria, J. P., Suárez Mascareño, A., Figueira, P., et al. 2022, *A&A*, **658**, A115
 Fuhrmeister, B., Lalitha, S., Poppenhaeger, K., et al. 2011, *A&A*, **534**, A133
 Garcia-Sage, K., Gloer, A., Drake, J. J., Gronoff, G., & Cohen, O. 2017, *ApJL*, **844**, L13
 Garraffo, C., Cohen, O., Drake, J. J., & Downs, C. 2013, *ApJ*, **764**, 32
 Garraffo, C., Drake, J. J., & Cohen, O. 2015a, *ApJ*, **813**, 40
 Garraffo, C., Drake, J. J., & Cohen, O. 2015b, *ApJL*, **807**, L6
 Garraffo, C., Drake, J. J., & Cohen, O. 2016a, *A&A*, **595**, A110
 Garraffo, C., Drake, J. J., & Cohen, O. 2016b, *ApJL*, **833**, L4
 Garraffo, C., Drake, J. J., Cohen, O., Alvarado-Gómez, J. D., & Moschou, S. P. 2017, *ApJL*, **843**, L33
 Garraffo, C., Drake, J. J., Dotter, A., et al. 2018, *ApJ*, **862**, 90
 Gastine, T., Morin, J., Duarte, L., et al. 2013, *A&A*, **549**, L5
 Gombosi, T. I. 2004, in *Physics of the Space Environment*, ed. T. I. Gombosi, Vol. 357 (Cambridge: Cambridge Univ. Press)
 Gratton, R., Zurlo, A., Le Coroller, H., et al. 2020, *A&A*, **638**, A120
 Haisch, B. M., Linsky, J. L., Bornmann, P. L., et al. 1983, *ApJ*, **267**, 280
 Jackson, A. P., Davis, T. A., & Wheatley, P. J. 2012, *MNRAS*, **422**, 2024
 Kavanagh, R. D., Vidotto, A. A., Klein, B., et al. 2021, *MNRAS*, **504**, 1511
 Kervella, P., Arenou, F., & Schneider, J. 2020, *A&A*, **635**, L14
 Kiraga, M., & Stepien, K. 2007, *AcA*, **57**, 149
 Kivelson, M. G., & Russell, C. T. 1995, *Introduction to Space Physics* (Cambridge: Cambridge Univ. Press), 586
 Klein, B., Donati, J.-F., Hébrard, É. M., et al. 2021, *MNRAS*, **500**, 1844
 Kopparapu, R. K., Ramirez, R., Kasting, J. F., et al. 2013, *ApJ*, **770**, 82
 Kopparapu, R. K., Ramirez, R. M., SchottelKotte, J., et al. 2014, *ApJL*, **787**, L29
 Kraft, R. P. 1967, *ApJ*, **150**, 551
 Morin, J., Donati, J.-F., Petit, P., et al. 2010, *MNRAS*, **407**, 2269
 Moschou, S.-P., Drake, J. J., Cohen, O., et al. 2019, *ApJ*, **877**, 105
 Noyes, R. W., Hartmann, L. W., Baliunas, S. L., Duncan, D. K., & Vaughan, A. H. 1984, *ApJ*, **279**, 763
 Pevtsov, A. A., Fisher, G. H., Acton, L. W., et al. 2003, *ApJ*, **598**, 1387
 Pizzolato, N., Maggio, A., Micela, G., Sciortino, S., & Ventura, P. 2003, *A&A*, **397**, 147
 Powell, K. G., Roe, P. L., Linde, T. J., Gombosi, T. I., & De Zeeuw, D. L. 1999, *JCoPh*, **154**, 284
 Reiners, A., & Basri, G. 2008, *A&A*, **489**, L45
 Réville, V., Brun, A. S., Matt, S. P., Strugarek, A., & Pinto, R. F. 2015, *ApJ*, **798**, 116
 Ribas, I., Bolmont, E., Selsis, F., et al. 2016, *A&A*, **596**, A111
 Sachdeva, N., van der Holst, B., Manchester, W. B., et al. 2019, *ApJ*, **887**, 83
 See, V., Lehmann, L., Matt, S. P., & Finley, A. J. 2020, *ApJ*, **894**, 69
 See, V., Matt, S. P., Finley, A. J., et al. 2019, *ApJ*, **886**, 120
 Ségransan, D., Kervella, P., Forveille, T., & Queloz, D. 2003, *A&A*, **397**, L5
 Shields, A. L., Ballard, S., & Johnson, J. A. 2016, *PhR*, **663**, 1
 Skumanich, A. 1972, *ApJ*, **171**, 565
 Suárez Mascareño, A., Faria, J. P., Figueira, P., et al. 2020, *A&A*, **639**, A77
 Toth, G., Sokolov, I. V., Gombosi, T. I., et al. 2005, *JGRA*, **110**, A12226
 Toth, G., van der Holst, B., Sokolov, I. V., et al. 2012, *JCoPh*, **231**, 870
 Turbet, M., Leconte, J., Selsis, F., et al. 2016, *A&A*, **596**, A112
 Vaiana, G. S., Cassinelli, J. P., Fabbiano, G., et al. 1981, *ApJ*, **245**, 163
 van der Holst, B., Sokolov, I. V., Meng, X., et al. 2014, *ApJ*, **782**, 81
 Vida, K., Oláh, K., Kóvári, Z., et al. 2019, *ApJ*, **884**, 160
 Vidotto, A. A., Jardine, M., Morin, J., et al. 2014, *MNRAS*, **438**, 1162
 Wargelin, B. J., Saar, S. H., Pojmański, G., Drake, J. J., & Kashyap, V. L. 2017, *MNRAS*, **464**, 3281
 Wood, B. E., Müller, H.-R., Zank, G. P., Linsky, J. L., & Redfield, S. 2005, *ApJL*, **628**, L143
 Wright, N. J., Drake, J. J., Mamajek, E. E., & Henry, G. W. 2011, *ApJ*, **743**, 48
 Yadav, R. K., Christensen, U. R., Morin, J., et al. 2015a, *ApJL*, **813**, L31
 Yadav, R. K., Christensen, U. R., Morin, J., et al. 2015b, *ApJL*, **813**, L31
 Yadav, R. K., Christensen, U. R., Wolk, S. J., & Poppenhaeger, K. 2016, *ApJL*, **833**, L28
 Zic, A., Murphy, T., Lynch, C., et al. 2020, *ApJ*, **905**, 23
 Zuluaga, J. I., & Bustamante, S. 2018, *P&SS*, **152**, 55